Unique crystallographic pattern in the macro to atomic structure of *Herdmania momus* vateritic spicules

Lee Kabalah-Amitai [a], Boaz Mayzel [c], Paul Zaslansky [d], Yaron Kauffmann [a], Peter Clotens [e], Boaz Pokroy [a,b,*]

[a] Department of Materials Science and Engineering, Technion – Israel Institute of Technology, 32000 Haifa, Israel
[b] Russell Berrie Nanotechnology Institute, Technion – Israel Institute of Technology, 32000 Haifa, Israel
[c] Department of Biology, Tel Aviv University, 69978 Tel Aviv, Israel
[d] Berlin – Brandenburg Center for Regenerative Therapies, Julius Wolff Institut, Charité – Universitätsmedizin, Berlin, Germany
[e] European Synchrotron Radiation Facility, BP 220, F-38043 Grenoble Cedex, France

ARTICLE INFO

ABSTRACT

Biogenic vaterite is extremely rare. The only known example of a completely vateritic mineralized structure is the spicule of the solitary ascidian, *Herdmania momus*. In characterizing the structure of these spicules, using state-of-the-art techniques such as synchrotron X-ray diffraction and synchrotron micro- and nanotomography, we observed a continuous structural pattern from the macro down to the micro, nano, and atomic scales. We show that the spicules demonstrate a unique architecture composed of micron-sized, hexagonally faceted thorns organized in partial spirals along the cylinder-like polycrystalline body of the spicule, and tilted from it at an angle of about 26°. This morphological orientation coincides with the crystallographic orientation relationship between each thorn and the polycrystals within the spicule. Hence the entire spicule grows along the [011] direction of vaterite while the individual thorns grow along the [001] direction. This, together with the presence of both inter- and intra-crystalline organic phases, beautifully displays the organism's ability to achieve perfect control of mineralization biologically while employing an unstable polymorph of calcium carbonate: vaterite.

1. Introduction

Organisms produce a variety of minerals for different functions (Weinkamer et al., 2013). In the course of building minerals in nature (biogenic minerals), organisms exert biological control mechanisms to choose the desired compound and specific polymorph (Falini et al., 1996; Gotliv et al., 2003) and to grow the crystals in a precise crystallographic orientation and morphology (Aizenberg et al., 1995a,b; Albeck et al., 1996; DeOliveira and Laursen, 1997; Heywood et al., 1990). Furthermore, each organism can grow a number of crystals to form a specific array, or alternatively a single crystal with various unexpected shapes (Aizenberg et al., 2003; Weiner and Addadi, 1997). Control over the morphology and shape selection of the specific polymorph is exerted over all scales from the macro to the atomic (Dunlop and Fratzl, 2010; Meldrum, 2003; Weiner and Addadi, 1997; Nudelman and Sommerdijk,

2012). Each biomineral has its own specifically desired function, which may be, for example, mechanical (Curry and Menon, 1976; Kamat et al., 2000; Mayer, 2005; Pokroy and Zolotoyabko, 2003), optical (Aizenberg et al., 2001), or magnetic (Mann et al., 1990).

Among the different minerals known to result from biomineralization, calcium carbonate ($CaCO_3$) is by far the most abundant (Lowenstam and Weiner, 1989). It is found in many organisms, serves a variety of functions, and exists in order of decreasing thermodynamic stability under normal conditions in the form of three anhydrous polymorphs: calcite, aragonite and vaterite. The last, vaterite, is metastable under normal conditions, and in biology or geology, if found at all it usually exists as a relatively small percentage of a mixture of different phases. Nevertheless, vaterite is very common in synthetic essays (Pokroy et al., 2006; Pouget et al., 2009; Xu et al., 2006). This makes biogenic vaterite difficult to characterize and, as a consequence, it has attracted relatively little research. It seems that biogenic vaterite almost always occurs either as a minority component of a larger formed structure or as an outcome of a faulty biological process. A few examples are found in eggshells of the green turtle (Lakshminarayanan et al., 2005), in otoliths of the coho salmon (Wehrmeister et al., 2010), in freshwater lackluster pearls (Qiao and Feng, 2007; Qiao et al., 2007, 2008), and in the abnormal growth of damaged mollusk

---

shells following their biological repair (Isaure et al., 2010). The sole example of biogenic vaterite that is deposited as the only mineral component of an organism's endoskeleton is found in the body spicules and tunic spicules of the solitary stolidobranch ascidian *Herdmania momus* (Kabalah-Amitai et al., 2013; Lowenstam and Abbott, 1975). These exquisite spicules are composed of micron-sized vaterite crystals.

1.1. The solitary ascidian H. momus

H. momus, initially named *Cynthia momus*, is a solitary ascidian with a rounded shape and a color ranging from dull white to pink-orange. It was first described in the Gulf of Suez by Savigny in 1816. Since then it has been found in many marine habitats world-wide, including the Red Sea, the Indian Ocean, the Malay Archipelago, Australia, Japan, the Caribbean region, Brazil and in recent decades the the eastern Mediterranean basin (Nishikawa, 2002; Van Name, 1945). *H. momus* is common in relatively shallow water at depths from 1 to 30 m, but has also been found at depths of 100–250 m (Nishikawa, 2002; Van Name, 1945). Its size varies according to site, from 4.5 cm in the Caribbean to 9 cm in the Mediterranean (Nishikawa, 2002; Van Name, 1945). The tunic is soft and often fouled by epibionts.

H. momus, like other ascidians, has a short motile larval phase and the adult is sessile. Once the free-swimming larva has settled, it metamorphoses and the newly settled ascidian starts to feed (Goodbody, 1993). They are filter feeders, obtaining their food by straining detritus particles, phytoplankton, and bacteria from the seawater. The two distinct cylindrical siphons are lined with characteristic red-pink and white bands (Singh et al., 2009). Large numbers of long calcium carbonate spicules (1–2.5 mm) are found in the mantle, siphons and branchial basket tissues ("body spicules"), while the spicules found in the tunic ("tunic spicules") are much smaller (100 μm) (Lambert, 1992).

These characteristic spicules were noted and described by Heller in 1878 as "transverse rows of spiny bristles", and by Herdman, who in 1882 noted the two types of "echinated spicules" (Nishikawa, 2002; Van Name, 1945). Both the body and the tunic spicules of *H. momus* were first analyzed and described in detail by Sluiter in 1885 (Lambert and Lambert, 1987). The genus *Herdmania* itself was originally established by Lahille in 1888 to include ascidian species with "calcareous needle-like spicules covered in rings of spines" (Nishikawa, 2002; Van Name, 1945). Lowenstam and Abbott (1975), using powder X-ray diffraction and infrared spectra analyses, demonstrated that both types of spicules biomineralized by *H. momus* are from vaterite, and not from aragonite or calcite as found in other ascidian species (Lowenstam and Abbott, 1975). Monniot later reported the presence of fluorine in *H. momus* vaterite spicules (Monniot et al., 1995). The most detailed descriptions of *H. momus* spicules and their mineralization process were by Gretchen and Charles Lambert (Lambert, 1992; Lambert and Lambert, 1987).

The large, spindle-shaped body spicules are typically 1–2 mm long. Each body spicule consists of 100 or more rows of overlapping fringing thorns (Lahille's "spines"), all oriented towards the "basal" end of the spicule (Lambert and Lambert, 1987). Individual fringing thorns are distinct and pointed at their tips, but in their basal region they are joined together by an extracellular inter-thorn matrix (Hare et al., 1954; Lambert, 1992).

The body spicules are formed inside long, multilayered extracellular sheaths, where they are closely packed in long strings. The sheaths are embedded throughout the mantle and are especially abundant in the region surrounding the stomach and intestine, as well as in the siphons. Dense clumps of body spicules are also found in the folds of the branchial basket. Spicule-containing sheaths in the body wall are wrapped around the body in various

directions. New spicules form only at the growing end of a sheath, and not between spicules that are already formed (Lambert, 1992). The body spicules remain in place and apparently continue to increase in size throughout the life of the organism. At the apical end of the spicule new rows of thorns are added, possibly as a result of extracellular mineral formation by a group of sclerocytes. New thorns may also form between older and larger ones. The pseudopodial sclerocytes are found between neighboring body spicules, and overlie the fringing thorns. The interconnecting pseudopodia of the sclerocytes form isolated compartments in which matrix is deposited and spicules develop (Lambert, 1992).

Tunic spicules are much smaller than body spicules, being only 100–160 μm long. A mature tunic spicule has 20–40 rows of fringing thorns all pointing "backwards", i.e., away from its tip and towards its mace-shaped end. The "posterior" end has tiny thorns pointing in all directions and one row of larger thorns pointing "forward". The tunic spicules begin their development in the tunic blood vessels. Following nucleation, each tunic spicule grows inside an organic envelope attached to the blood vessel's inner wall. Within 4–5 days, once they have reached a length of 120–160 μm, they leave their surrounding organic envelope and migrate from the tunic blood vessels in which they were formed. They pass, point first, through the vessel walls to the tunic surface, from which they ultimately protrude, anchored to the tunic by their mace-like end (Lambert and Lambert, 1987).

Although these spicules have been known for many years, the only characterization published so far is the macro-scale shape of both spicule types. In this study, by utilizing state-of-the-art high-resolution characterization techniques, we characterized the nanostructure, microstructure, shape and morphology of the body spicules and their individual thorns as well as the three-dimensional relative organization of the crystals that constitute the spicules.

2. Materials and methods

2.1. Spicule separation

H. momus specimens from the Red Sea were collected by scuba diving from marine floats in Eilat at the northern tip of the Gulf of Aqaba, Israel. The *H. momus* specimens collected were all between 4 and 6 cm long. They were cut into small tissue pieces and treated with 7% sodium hypochlorite to remove the organic matter. The NaOCl was replaced frequently and the vials were shaken gently for 6 weeks until all organic matter was totally removed. Body spicules, 1–2 mm in length and ~20 μm in diameter, were filtered to remove debris and washed at least 3 times in 100% ethanol.

To characterize the spicules we examined their shape in samples from the nano to the millimeter scale, and their crystallographic orientation, which reflects the spicule's morphology. We also examined them for the presence of an organic phase as intra- or inter-crystalline molecules. Scanning electron microscopy (SEM), transmission electron microscopy (TEM), and synchrotron radiation diffraction were utilized for the characterization process.

2.2. Sample preparation

2.2.1. SEM sample preparation

Spicules were placed on an aluminum SEM sample holder directly from storage in pure ethanol. Samples were air-dried and then coated with nanometer-thick amorphous carbon.

2.2.2. TEM sample preparation

Spicules were prepared as for the SEM samples. After they were mounted and coated, a dual-beam Focused Ion Beam (FIB) was

used to prepare thin lamellae in different directions. This was done in several steps. First, the region of interest on the spicule was coated with up to 3 μm of platinum by electron-beam and ion-beam deposition inside the FIB vacuum chamber. Next, each thin lamella was further cut and thinned so that TEM specimens could be lifted off the sample holder and transferred to a molybdenum TEM grid for further thinning with a gallium ion beam.

2.2.3. Samples for synchrotron radiation 3D tomography imaging

A single *H. momus* spicule was placed on a glass needle with a micron-sized tip.

2.3. Characterization

For SEM characterization we used a Zeiss Ultra Plus Field Emission Gun SEM at an acceleration voltage of 4 or 1.2 kV, and equipped with an in-lens secondary electron detector. We also used the four-quadrant angle selective backscattered-electron (AsB) detector, which allows imaging in orientation, topographic, or composition contrast modes.

TEM images (e.g. bright field (BF), dark field (DF)), S/TEM (Scanning/Transmission electron microscopy), phase-contrast High Resolution TEM (HRTEM) images were obtained, and diffractions were performed, with an FEI Tecnai G2 T20 S-Twin TEM and high-resolution aberration corrected FEI Titan 80–300 keV S/TEM at acceleration voltages of 300, 200 or 80 kV.

Synchrotron radiation 3D tomography imaging was performed both on ID22NI of the European Synchrotron Radiation Facility (ESRF, Grenoble, France) and on the BAM-line at the BESSY-II storage ring (Helmholtz-Zentrum Berlin, Germany).

2.4. Data analysis

2.4.1. Electron diffraction

To analyze the electron diffraction data collected via TEM we used the JEMS Electron Microscopy Software Package (Version 3.1102W2006, Copyright: P. Stadelmann, 1999–2006), a program for the simulation of electron diffraction patterns and high-resolution images.

2.4.2. Phase contrast-enhanced microtomography

The high-resolution microtomography set-up of the BAMline at the BESSY-II storage ring was operated as described elsewhere (Bentov et al., 2012; Riesemeier et al., 2009). For our samples we used energy of 20 keV and obtained 360 projections spanning 180° around the sample axis. We used an effective pixel size of 438 nm and positioned the detector system 50 mm behind the sample. Data were normalized using a custom-written code and then reconstructed by filtered back-projection using an ESRF cone (Mirone et al., 2009). High Speed Tomographic (PyHST) reconstruction data manipulation and visualization were performed with ImageJ (Schneider et al., 2012) and CTvox (micro-MRI, 2012).

2.4.3. Nanotomography

This method is described in detail elsewhere (see e.g. (Langer et al., 2012). For 3D X-ray phase nanotomography we employed no special sample preparation other than mounting the samples upright on a stud. Nanotomography was performed at the nano-imaging station ID22NI of the ESRF, using an X-ray spot focus with an X-ray energy of 29.5 keVa, obtained from a combination of multilayer-coated mirrors (Kirkpatrick–Baez crossed mirrors). The samples were set at a small distance downstream of the focus and the transmitted intensities were recorded using the imaging system of the beamline. For each scan, 1999 images were recorded while the sample was incrementally rotated by 360° around the vertical sample axis. To resolve phase ambiguities and obtain ultra-high-resolution details, datasets were obtained at four sample-source distances. ESRF custom code was used, first to retrieve the phase (estimating a delta/beta ratio of 370 for calcium carbonate) by holotomographic reconstruction (Cloetens et al., 1999), and then to reconstruct volumes as described for the phase contrast-enhanced microtomography data.

3. Results and discussion

3.1. H. momus body spicule: Ultra-and micro-structure

H. momus spicules were examined by synchrotron high-resolution powder diffraction on ID31 of the ESRF and the diffraction spectra were treated with Rietveld structure refinement. This
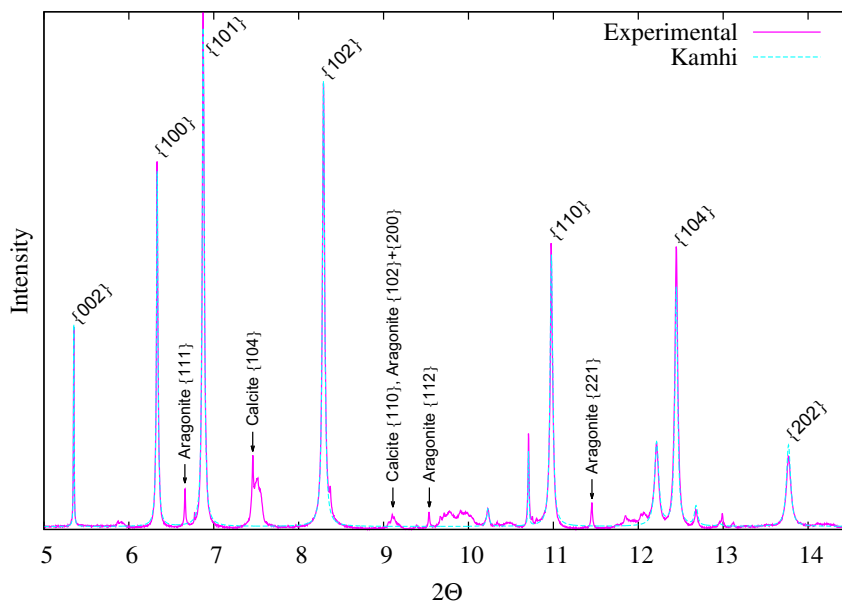
Fig.1. High-resolution synchrotron powder diffraction spectrum obtained on ID31 of the ESRF (pink line) and the calculated spectrum according to Kamhi's structural model (purple line).
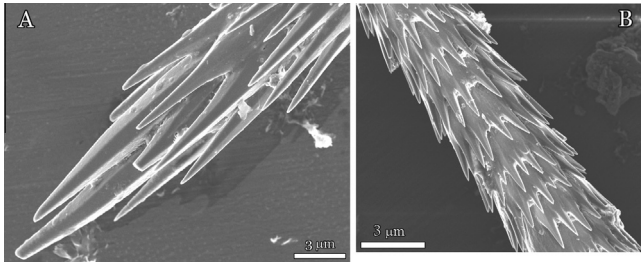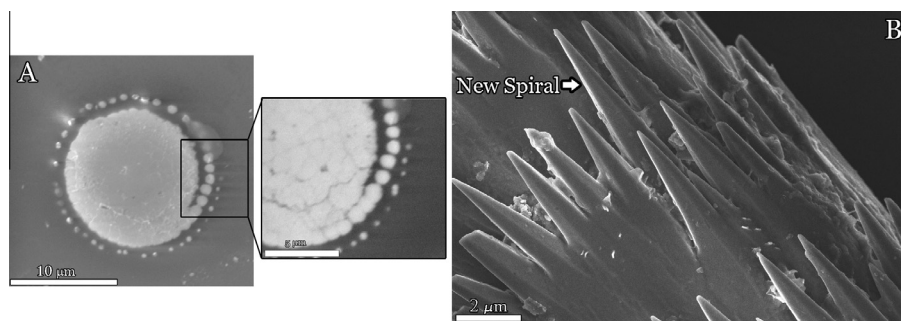
Fig.2. (A, B) SEM images of the *Herdmania momus* body spicule (High voltage, (HV) = 4 kV).
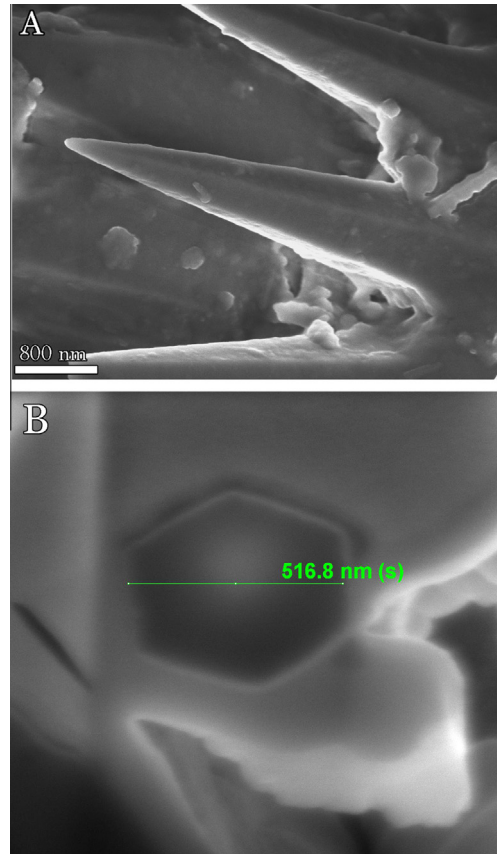
analysis confirmed that the spicules indeed consist exclusively of vaterite. Over the past century there has been a continuous debate on the crystal structure of vaterite (Wehrmeister et al., 2010), however very recently we have shown that the reason for this ongoing debate is that crystals of vaterite contain at least two different crystal structures that coexist (Kabalah-Amitai et al., 2013). Despite this recent finding, our X-ray diffraction experimental data convincingly showed that of all the proposed crystal structures the model of Kamhi (1963) still provides the best fit (Fig. 1) due to the fact that the major crystalline phase is that of Kamhi, and we therefore refer to the vaterite polycrystals as in the Kamhi model throughout this paper. Interestingly, although under ordinary conditions vaterite is a metastable phase, the biogenic vaterite comprising these spicules is stable in seawater and has demonstrated stability in 100% ethanol over several years. Extensive work on the stability of biogenic vaterite was done by Prof. Steve Weiner (Weizmann Institute) and by the late Prof. Heinz A. Lowenstam both utilizing IR spectroscopy (Lowenstam and Abbott, 1975).

The SEM image presented in Fig. 2 is in agreement with previous observations (Lowenstam and Abbott, 1975) that the body spicule of *H. momus* is 1–2 mm in length and that the main body has chiefly a cylindrical shape of 15–30 μm diameter. On the spicule's circumference, micron-sized faceted single crystalline thorns are distributed in a particular order, which was subsequently found to be an arrangement of half spirals (i.e., of pseudo-spiral structures) along the spicule length (Fig. 3 and video file, Supplementary data 1). Each micron-sized thorn has a hexagonal cross-section (Fig. 4), which coincides with the hexagonal symmetry of the major structural model of Kamhi (1963) and seem to diffract as a single crystal.

The material within the spicule's main body consists of pseudo-hexagonal polycrystalline vaterite crystals that are much smaller than the thorns. This was also pointed out by (Lowenstam and Abbott, 1975) and can be clearly seen upon HRSEM imaging (Fig. 3A
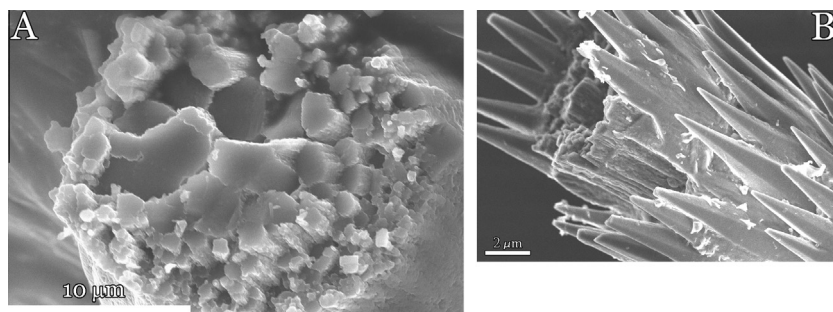

Fig.4. (A) SEM image (HV = 5 kV) showing the hexagonally faceted thorns. (B) A FIB slice perpendicular to the *c*-axis (main axis of a thorn) showing the hexagonal cross-section ((s) indicates a measurement value corrected to account for specimen tilting).

and Fig. 5A). The ordered polycrystalline structure of the *H. momus* spicules distinguishes them from many other calcitic spicules, such as those of the sea urchin, which exhibit a single-crystalline structure (Politi et al., 2008; Raz et al., 2003). This intriguing difference prompted us to study the crystallographic orientations between the crystals in the polycrystalline core and the single thorns and to understand their underlying design pattern and the 3D crystallographic orientations of these crystals.

To prepare samples of the main spicule body for TEM investigation we cut the main body of the spicule at two orthogonal directions (along the spicule's main axis (*z*-axis) and perpendicular to it,

Fig.3. SEM characterization of the pseudo-spiral organization of thorns. (A) Cross-section of a polished spicule, imaged in back-scattered electron (BSE) imaging mode. (B) Segment of a single spicule in which the pseudo-spiral organization of thorns can be observed in secondary electron (SE) imaging mode. Two thorns at the initiation of a new spiral organization of thorns is marked by a white arrow. In both (A) and (B) the spirals are marked. The 3D pseudo-spiral organization by synchrotron micro-tomography can be seen in a video file (Supplementary data 1).
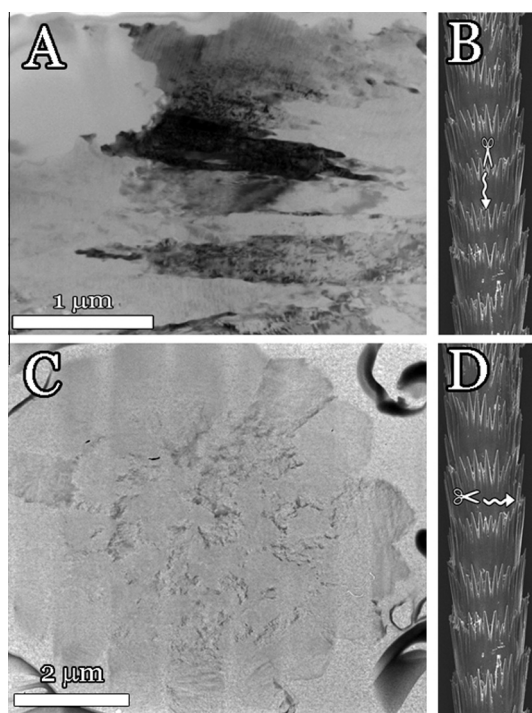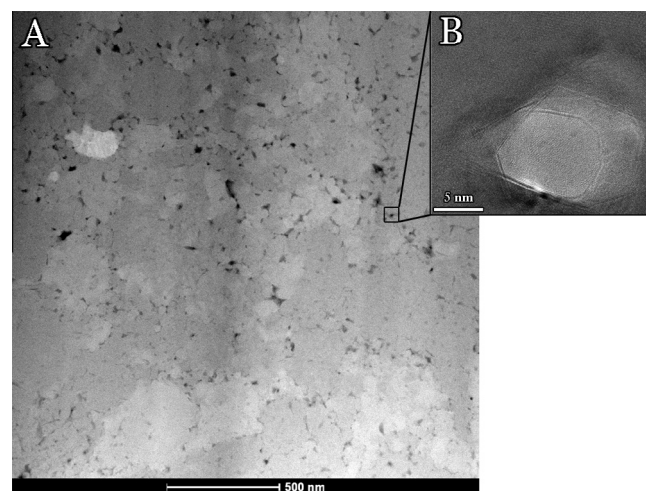
Fig.5. HRSEM image of vateritic polycrystals within the spicule's main body. (A) Edge-on view of a cross-section prepared perpendicular to the main spicule's long axis. (B) Side view of the spicule, showing the polycrystals within the spicule.

Fig.6. TEM images. (A) TEM diffraction contrast image in bright-field mode of a sample cut parallel to the z-axis, revealing micron-sized crystals. (B) Illustration of the parallel cut made in the center of the spicule. (C) TEM image at low magnification, bright field mode out of zone axis of a sample cut perpendicularly to the z-axis. (D) Illustration of the perpendicular cut made in the center of the spicule.
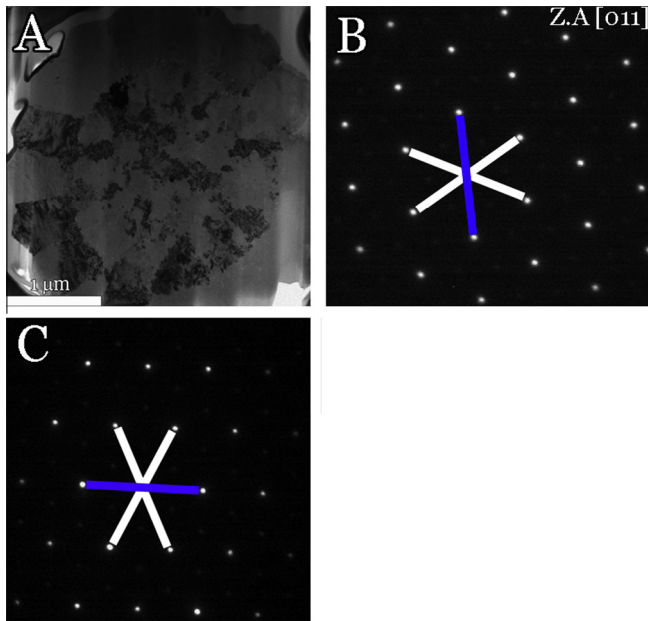

Fig.7. (A) STEM-HAADF mode (HV = 100 kV) imaging of a cross-section perpendicular to the z-axis of the spicule's main body revealing crystals with diameters in the submicron scale (B) Nanosized pores can be seen between the polycrystals.

polycrystals (Fig. 7). The origin of these two pore types is as yet unknown. We suspect, despite the absence of corroborating evidence that they may have been caused by one or both of the following processes: a decrease in volume as a result of crystallization through an amorphous precursor (Aizenberg et al., 2003; Fratzl et al., 2010), or accumulation of organic molecules that were destroyed in the process of TEM sample preparation.

3.2. Crystallographic orientation of the spicule: Atomic scale

As mentioned above, as yet there is no consensus on the atomic structure of vaterite. We found, that both synchrotron X-ray powder diffraction and TEM electron diffraction and imaging indicate that compared to the proposed atomic structures, the atomic model proposed by Kamhi (1963) gives by far the best fit to the experimental data. This was affirmed in our study by the use of the Rietveld refinement (with goodness of fit χ^2 = 13; see Fig. 1).

According to Kamhi's atomic model, the unit cell of vaterite has hexagonal symmetry with a = 4.13 Å and c = 8.49 Å. It would be rational to assume that the c-axis is parallel to the z-axis of the spicule; however this is not the case for the spicule of *H. momus*. Solving the electron diffraction pattern from a sample cut perpendicular to the z-axis shows that the spicule along axis z is not parallel to the crystallographic c-axis but rather coincides with the [011] direction (Fig. 8). The individual thorns, however, do grow along the vateritic c-axis coinciding with the [001] direction).

as seen in Fig. 6). These cuts were made with a FIB (see Methods section) and were needed in order to measure the dimensions of the crystals and to understand their relative crystal orientation. TEM imaging of the two samples (Fig. 6A, C) shows that the polycrystals in the main body are elongated along the z-axis i.e., in the same direction as that of the spicule's long axis and are much narrower perpendicular to it. The cut parallel to the z-axis shows that each crystal in the main body is a few microns long (Fig. 6A). By comparison, their diameter (i.e., in the perpendicular direction) is on the submicron scale, as their width ranges over a few hundreds of nanometers (Fig. 7). In addition, because this spicule is a biogenic sample it was not surprising to detect, on further observation, that randomly distributed between the polycrystals in the main body there were two different types of pores: (1) micronscale elongated pores (parallel to the z-axis; video files in Supplementary Data 2), and (2) faceted nanoscale pores between the

Fig.8. (A) TEM image in bright-field mode (diffraction contrast) of a sample cut perpendicular to the z-axis. (B) Electron diffraction taken from one of the crystals (point 1) in (A). (C) Electron diffraction taken from another crystal (point 2) in (A). When the beam is translated between different crystals without altering the sample tilt within the TEM, the diffraction pattern rotates within the image plane, but—as can be seen in (A) and (B) the sample is maintained within Z.A [0 1 1] (the blue line marks a specific d-space in both diffraction patterns and the other white lines mark other two d-spacings. The comparison between (B) and (C) illustrates the relative rotation of different crystals in the plane perpendicular to the main spicule axis (z-axis).

These findings correlate with the hexagonally shaped cross-section of the thorns.

All the polycrystals in the spicule's main body grow along the [0 1 1] direction, but relative to the neighboring crystals they are rotated in the plane perpendicular to the z-axis. The rotation can be detected by translating the TEM sample under the beam while at the same time observing the changes in the electron diffraction pattern. Fig. 9 shows electron diffractions from two different crystals. When one crystal is in Z.A a clear diffraction pattern is obtained. However, when the sample under the beam is translated to obtain electron diffraction from a different crystal without tilting the sample, it is clear from the corresponding diffraction pattern that the second crystal is not in Z.A. Therefore, to achieve a diffraction pattern from the second crystal, the sample must be tilted to bring the second crystal into Z.A.

Our TEM observations from the polycrystalline region within the spicule body indicated that the polycrystals are all co-oriented in the z-axis along the [0 1 1] direction (Fig. 8), but that perpendicular to the z-axis they are not crystallographically aligned (Fig. 9).

Using synchroton microtomography (micro-CT) we obtained a slice view of an entire spicule, demonstrating both the polycrystalline (internal) region and the outer large thorns. This enabled us to measure non-destructively the angle between the thorns and the spicule's long axis (i.e., between the c-axis and the z-axis). This was found to be $26° \pm 1°$ (Fig. 10). In the vaterite crystallographic structure (Kamhi (1963) model) the angle between the [0 0 1] and [0 1 1] directions is exactly 26°. This further supports the orientation relationship that we obtained by electron diffraction. This orientation relationship, together with the observed 3D organization, corroborates the extremely interesting likelihood that the thorn growth is intimately associated with the polycrystalline internal region or even nucleates on the polycrystalline core.

3.3. Organic phase in the H. momus body spicule

Two types of organic phase, inter- and intracrystalline, are known to exist in biogenic minerals. The first serves as an organic substrate for mineral nucleation and growth, and may even operate as a membrane that selectively chooses the reactants for mineral nucleation and growth (Weiner and Addadi, 1997). Such
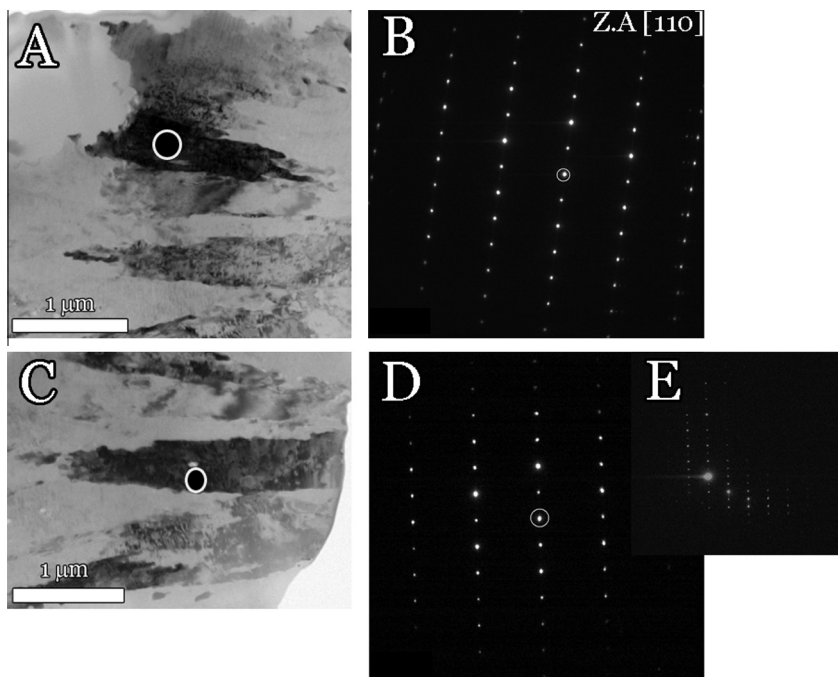
Fig.9. Electron diffractions and their corresponding TEM images of a sample cut parallel to the z-axis (bright-field mode). (A, C) bright-field images where the black contrast crystal is the diffracting one (marked with a white circle). (B) Electron diffraction from crystal # 1 when in Z.A. (D) Electron diffraction from crystal # 2 when the beam was only translated away from crystal # 1. The electron diffraction is not in Z.A and only additional tilting will bring crystal # 2 to Z.A. (E) Electron diffraction from crystal # 2 in Z.A. (When crystal # 1 is in Z.A, crystal # 2 is not in Z.A as can be seen from diffractions (B) and (D)).
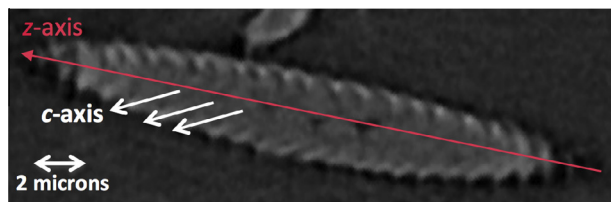
Fig.10. Micro-CT-computed internal slice of the spicule revealing an angle of ~26° between the main axis of the thorns and the main axis of the spicule.
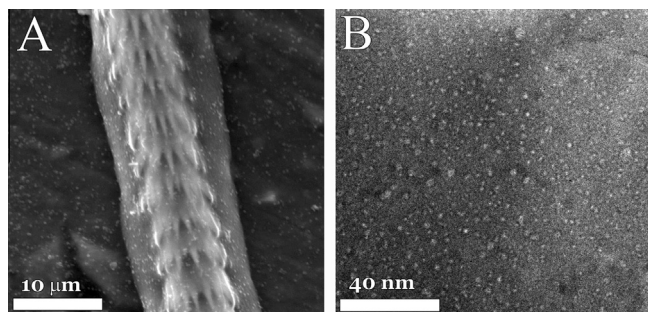
Fig.11. (A) SEM image of the intercrystalline organic phase covering the spicule. (B) HRTEM bright-field image of intracrystalline organic phase.

nucleation and growth modify the atomic structure and texture of the crystals (Berman et al., 1988, 1993; Pokroy et al., 2006), (Borukhin et al., 2012).

In this study we observed both types of organic phase in the *H. momus* body spicule via electron microscopy. Each spicule was seen to be covered with an organic sheath (Fig. 11A). To observe the intracrystalline organic phase, we prepared TEM samples from a single thorn. Of all the crystallographic directions examined, only a cut made perpendicular to the main axis of a thorn (*c*-axis) enabled us to probably detect, via bright-field high-resolution TEM, the intracrystalline organic phase (Fig. 11B). The fact that these bright spots were observed only perpendicular to the *c*-axis coincides with our unpublished XRD observations that indicate that the intracrystalline molecules are probably mainly located on planes perpendicular to the *c*-axis. However at this point we cannot completely eliminate the possibility that the bright spots are nano-voids. This was clearly due to the fact that in bright-field mode the contrast is obtained by *z*-contrast as well as by diffraction contrast. Since the organic aggregates are brighter, they must be composed of materials with lower atomic numbers than the vaterite matrix. Hence, it is evident that if indeed these spots are organisms most of the intracrystalline organic molecules are located on the (0 0 1) plane of the vateritic thorns. Other studies have also shown such TEM images when intracrystalline organics were located within a mineral (Kim et al., 2011; Younis et al., 2012).

4. Conclusions

The vateritic spicules of *H. momus* provide a fascinating example that proves once again the precise control that organisms exert on all the structural parameters of their crystals (polymorph, morphology and crystal orientation) through both inter- and intracrystalline organic phases. The resulting spicule structure in this species has a rotated character around the spicule's elongated direction (*z*-axis) from the rotated elongated polycrystals of the main body to the hexagonal thorns that form a partially spiral array. Most interestingly, the spicule's growth is not along the [0 0 1]

direction, as would be expected because this is the *c*-axis of the unit cell, but rather along the [0 1 1] direction. There is a clear 3D orientation relationship between the outer thorns and the inner crystals. At this point we do not know the specific mechanism of formation of the spicule 3D crystallography, and although there is no direct evidence of an amorphous precursor phase like that known to be present in other calcific spicules (Politi et al., 2008; Raz et al., 2003), we cannot rule out this possibility. Further investigation will be performed in an attempt to gain a better understanding of these mechanisms.

Appendix A. Supplementary data

Supplementary data associated with this article can be found, in the online version, at http://dx.doi.org/10.1016/j.jsb.2013.05.002.

References

Aizenberg, J., Muller, D.A., Grazul, J.L., Hamann, D.R., 2003. Direct fabrication of large micropatterned single crystals. Science 299, 1205–1208.

Aizenberg, J., Tkachenko, A., Weiner, S., Addadi, L., Hendler, G., 2001. Calcitic microlenses as part of the photoreceptor system in brittlestars. Nature 412, 819–822.

Aizenberg, J., Hanson, J., Koetzle, T.F., Leiserowitz, L., Weiner, S., Addadi, L., 1995a. Biologically induced reduction in symmetry – a study of crystal texture of calcitic sponge spicules. Chem. Eur. J. 1, 414–422.

Aizenberg, J., Hanson, J., Ilan, M., Leiserowitz, L., Koetzle, T.F., Addadi, L., Weiner, S., 1995b. Morphogenesis of calcitic sponge spicules – a role for specialized proteins interacting with growing crystals. Faseb J. 9, 262–268.

Albeck, S., Addadi, L., Weiner, S., 1996. Regulation of calcite crystal morphology by intracrystalline acidic proteins and glycoproteins. Connect. Tissue Res. 35, 365–370.

Bentov, S., Zaslansky, P., Al-Sawalmih, A., Masic, A., Fratzl, P., Sagi, A., Berman, A., Aichmayer, B., 2012. Enamel-like apatite crown covering amorphous mineral in a crayfish mandible. Nat. Commun. 3.

Berman, A., Addadi, L., Weiner, S., 1988. Interactions of sea-urchin skeleton macromolecules with growing calcite crystals – a study of intracrystalline proteins. Nature 331, 546–548.

Berman, A., Hanson, J., Leiserowitz, L., Koetzle, T.F., Weiner, S., Addadi, L., 1993. Biological control of crystal texture: a widespread strategy for adapting crystal properties to function. Science 259, 776–779.

Borukhin, S., Bloch, L., Radlauer, T., Hill, A.H., Fitch, A.N., Pokroy, B., 2012. Screening the incorporation of amino acids into an inorganic crystalline host: the case of calcite. Adv. Funct. Mater. 22, 4216–4224.

Cloetens, P., Ludwig, W., Baruchel, J., Guigay, J.-P., Pernot-Rejmánková, P., Salomé-Pateyron, M., Schlenker, M., Buffière, J.-Y., Maire, E., Peix, G., 1999. Hard X-ray phase imaging using simple propagation of a coherent synchrotron radiation beam. J. Phys. D Appl. Phys. 32, A145.

Curry, J., Menon, M.P., 1976. Determination of traces of mercury using radioactive zinc dithizonate as a reagent. J. Radioanal. Chem. 34, 319–327.

DeOliveira, D.B., Laursen, R.A., 1997. Control of calcite crystal morphology by a peptide designed to bind to a specific surface. J. Am. Chem. Soc. 119, 10627–10631.

Dunlop, J.W.C., Fratzl, P., 2010. Biological composites. In: Clarke, D.R., et al., (Eds.), Annual Review of Materials Research, Annual Reviews, Palo Alto. Vol. 40, pp. 1–24.

Falini, G., Albeck, S., Weiner, S., Addadi, L., 1996. Control of aragonite or calcite polymorphism by mollusk shell macromolecules. Science 271, 67–69.

Fratzl, P., Fischer, F.D., Svoboda, J., Aizenberg, J., 2010. A kinetic model of the transformation of a micropatterned amorphous precursor into a porous single crystal. Acta Biomater. 6, 1001–1005.

Goodbody, I.M., 1993. The biology of ascidia nigra (Savigny). II. The development and survival of young ascidians. Biol. Bull. 124, 31–44.

Gotliv, B.A., Addadi, L., Weiner, S., 2003. Mollusk shell acidic proteins: in search of individual functions. ChemBioChem 4, 522–529.

Hare, E.F., Shafrin, E.G., Zisman, W.A., 1954. Properties of films of adsorbed fluorinated acids. J. Phys. Chem. 58, 236–239.

Heywood, B.R., Sparks, N.H.C., Shellis, R.P., Weiner, S., Mann, S., 1990. Ultrastructure, morphology and crystal-growth of biogenic and synthetic apatites. Connect. Tissue Res. 25, 103–119.

Isaure, M.-P., Sarret, G., Harada, E., Choi, Y.-E., Marcus, M.A., Fakra, S.C., Geoffroy, N., Pairis, S., Susini, J., Clemens, S., Manceau, A., 2010. Calcium promotes cadmium elimination as vaterite grains by tobacco trichomes. Geochim. Cosmochim. Acta 74, 5817–5834.

Kabalah-Amitai, L., Mayzel, B., Kauffmann, Y., Fitch, A.N., Bloch, L., Gilbert, P.U.P.A., Pokroy, B., 2013. Vaterite crystals contain two interspersed crystal structures. Science 340, 454–457.

Kamat, S., Su, X., Ballarini, R., Heuer, A.H., 2000. Structural basis for the fracture toughness of the shell of the conch Strombus gigas. Nature 405, 1036–1040.

Kamhi, S., 1963. On the structure of vaterite CaCO$_3$. Acta Crystallogr. 16, 770–772.

Kim, Y.Y., Ganesan, K., Yang, P.C., Kulak, A.N., Borukhin, S., Pechook, S., Ribeiro, L., Kroger, R., Eichhorn, S.J., Armes, S.P., Pokroy, B., Meldrum, F.C., 2011. An artificial biomineral formed by incorporation of copolymer micelles in calcite crystals. Nat. Mater. 10, 890–896.

Lakshminarayanan, R., Chi-Jin, E.O., Loh, X.J., Kini, R.M., Valiyaveettil, S., 2005. Purification and characterization of a vaterite-inducing peptide, pelovaterin, from the eggshells of *Pelodiscus sinensis* (Chinese soft-shelled turtle). Biomacromolecules 6, 1429–1437.

Lambert, G., 1992. Ultrastructural aspects of spicule formation in the solitary ascidian *Herdmania momus* (Urochordata, Ascidiacea). Acta Zoologica 73, 237–245.

Lambert, G., Lambert, C.C., 1987. Spicule formation in the solitary ascidian, Herdmania momus. J. Morphology 192, 145–159.

Lowenstam, H., Abbott, D., 1975. Vaterite: a mineralization product of the hard tissues of a marine organism (Ascidiacea). Science 188, 363–365.

Lowenstam, H., Weiner, S., 1989. On Biomineralization. Oxford University Press, USA.

Mann, S., Sparks, N.H.C., Frankel, R.B., Bazylinski, D.A., Jannasch, H.W., 1990. Biomineralization of ferrimagnetic greigite (Fe$_3$S$_4$) and iron pyrite (FeS$_2$) in a Magnetotactic Bacterium. Nature 343, 258–261.

Langer, Max, Pacureanu, Alexandra, Suhonen, Heikki, Grimal, Quentin, Cloetens, Peter, Peyrin, Françoise, 2012. X-ray phase nanotomography resolves the 3D human bone ultrastructure. PLoS One 7, e35691.

Mayer, G., 2005. Rigid biological systems as models for synthetic composites. Science 310, 1144–1147.

Meldrum, F.C., 2003. Calcium carbonate in biomineralisation and biomimetic chemistry. Int. Mater. Rev. 48, 187–224.

micro-MRI, M.o.C.l.i.w.m.-C.a., 2012. Vande Velde, G., Dresselaers, T., Verbeken, E., Lagrou, K., Himmelreich, U., http://www.skyscan.be/products/downloads.htm#CTvox.

Mirone, A., Wilcke, R., Hammersley, A., Ferrero, C., 2009. PyHST – High Speed Tomographic Reconstruction. http://www.esrf.eu/Instrumentation/software/data-analysis/.

Monniot, F., Clement, P., Souron, J.P., 1995. The ubiquity of fluorine amidst the taxonomic and mineralogical diversity of ascidian spicules. Biochem. Syst. Ecol. 23, 129–137.

Nishikawa, T., 2002. Revision of the ascidian genus Herdmania(Urochordata: Ascidiacea) inhabiting japanese waters. Species Divers 7, 217–250.

Nudelman, F., Sommerdijk, N., 2012. Biomineralization as an inspiration for materials. Chem. Angew. Chem.Int. Ed. 51, 6582–6596.

Pokroy, B., Zolotoyabko, E., 2003. Microstructure of natural plywood-like ceramics: a study by high-resolution electron microscopy and energy-variable X-ray diffraction. J. Mater. Chem. 13, 682–688.

Pokroy, B., Zolotoyabko, E., Adir, N., 2006. Purification and functional analysis of a 40 kD protein extracted from the *Strombus decorus persicus* mollusk shells. Biomacromolecules 7, 550–556.

Politi, Y., Metzler, R.A., Abrecht, M., Gilbert, B., Wilt, F.H., Sagi, I., Addadi, L., Weiner, S., Gilbert, P., 2008. Transformation mechanism of amorphous calcium carbonate into calcite in the sea urchin larval spicule. Proc. Natl. Acad. Sci. U. S. A. 105, 17362–17366.

Pouget, E.M., Bomans, P.H.H., Goos, J.A.C.M., Frederik, P.M., de With, G., Sommerdijk, N.A.J.M., 2009. The initial stages of template-controlled caco3 formation revealed by Cryo-TEM. Science 323, 1455–1458.

Qiao, L., Feng, Q.L., 2007. Study on twin stacking faults in vaterite tablets of freshwater lacklustre pearls. J. Cryst. Growth 304, 253–256.

Qiao, L., Feng, Q.-L., Li, Z., 2007. Special vaterite found in freshwater lackluster pearls. Cryst. Growth Des. 7, 275–279.

Qiao, L., Feng, Q.L., Liu, Y., 2008. A novel bio-vaterite in freshwater pearls with high thermal stability and low dissolubility. Mater. Lett. 62, 1793–1796.

Raz, S., Hamilton, P.C., Wilt, F.H., Weiner, S., Addadi, L., 2003. The transient phase of amorphous calcium carbonate in sea urchin larval spicules: The involvement of proteins and magnesium ions in its formation and stabilization. Adv. Funct. Mater. 13, 480–486.

Riesemeier, H., Rack, A., Zabler, S., Goebbels, J., Müller, B.R., Banhart, J., 2009. The synchrotron-based imaging station for micro-radiography and-tomography at the BAMline (BESSY). J. Phys.Conf. Ser. 186, 012047.

Schneider, C.A., Rasband, W.S., Eliceiri, K.W., 2012. NIH Image to ImageJ: 25 years of image analysis. Nat. Methods 9, 671–675.

Singh, T., Tsagkogeorga, G., Delsuc, F., Blanquart, S., Shenkar, N., Loya, Y., Douzery, E., Huchon, D., 2009. Tunicate mitogenomics and phylogenetics: peculiarities of the *Herdmania momus* mitochondrial genome and support for the new chordate phylogeny. BMC Genomics 10, 534.

Van Name, W.G., 1945. The North and South American ascidians. B. Am. Mus. Nat. Hist. 84.

Wehrmeister, U., Soldati, A.L., Jacob, D.E., Häger, T., Hofmeister, W., 2010. Raman spectroscopy of synthetic, geological and biological vaterite: a Raman spectroscopic study. J. Raman Spectrosc. 42, 193–201.

Weiner, S., Addadi, L., 1997. Design strategies in mineralized biological materials. J. Mater. Chem. 7, 689–702.

Weinkamer, R., Dunlop, J.W.C., Brechet, Y., Fratzl, P., 2013. All but diamonds Biological materials are not forever. Acta Mater. 61, 880–889.

Xu, A.W., Antonietti, M., Colfen, H., Fang, Y.P., 2006. Uniform hexagonal plates of vaterite CaCO3 mesocrystals formed by biomimetic mineralization. Adv. Funct. Mater. 16, 903–908.

Younis, S., Kauffmann, Y., Bloch, L., Zolotoyabko, E., 2012. Inhomogeneity of nacre lamellae on the nanometer length scale. Cryst. Growth Des. 12, 4574–4579.